Emergence of a competing stripe phase near the Mott transition in Ti-doped bilayer calcium ruthenates

Ashish Gangshettiwar [1,*] Yanglin Zhu,[2,*] Zhanzhi Jiang [1] Jin Peng,[3] Yu Wang,[2,3] Jiaming He,[4] Jianshi Zhou,[4] Zhiqiang Mao,[2,3] and Keji Lai [1,†]

[1]*Department of Physics, University of Texas at Austin, Austin, Texas 78712, USA*
[2]*Department of Physics, The Pennsylvania State University, University Park, Pennsylvania 16802-6300, USA*
[3]*Department of Physics, Tulane University, New Orleans, Louisiana 70118, USA*
[4]*Department of Mechanical Engineering, University of Texas at Austin, Austin, Texas 78712, USA*

We report the nanoscale imaging of Ti-doped bilayer calcium ruthenates during the Mott metal-insulator transition by microwave impedance microscopy. Different from a typical first-order phase transition where coexistence of the two terminal phases takes place, a new metallic stripe phase oriented along the in-plane crystalline axes emerges inside both the *G*-type antiferromagnetic insulating state and the paramagnetic metallic state. The effect of this electronic state can be observed in macroscopic measurements, allowing us to construct a phase diagram that takes into account the energetically competing phases. Our work provides a model approach to correlate the macroscopic properties and mesoscopic phase separation in complex oxide materials.

The Ruddlesden-Popper series of alkaline-earth-metal ruthenates $(Sr, Ca)_{n+1}Ru_nO_{3n+1}$ display a wealth of fascinating behaviors that are representative of strongly correlated systems [1]. Compared with the Sr-based compounds [2,3], the metallicity of the Ca-based counterparts, if any, is much weaker due to the more distorted crystal structures [1]. For instance, $CaRuO_3$ ($n = \infty$) is a paramagnetic "bad" metal (PM-M) close to the antiferromagnetic (AFM) instability [4], whereas the single-layer ($n = 1$) Ca_2RuO_4 is a *G*-type AFM Mott insulator (*G*-AFM-I) at room temperature and undergoes a metal-insulator transition (MIT) at $T_{MIT} = 357$ K [5]. The intermediate member of bilayer ($n = 2$) $Ca_3Ru_2O_7$ is more complex, showing a magnetic transition at $T_N = 56$ K and an MIT at $T_{MIT} = 48$ K [6–10]. The magnetic ordering below T_N is of *A*-type AFM, i.e., ferromagnetic bilayers stacked antiferromagnetically along the *c* axis, and the moments switch from the *a* axis (denoted as AFM-*a*) to the *b* axis (AFM-*b*) upon cooling, as illustrated in Fig. 1(a) [10]. Moreover, the small Fermi pocket in the AFM-*a/b* phases [11] is suppressed by isovalent Ti doping into the Ru site through bandwidth reduction, which drives the ground state of $Ca_3(Ru_{1-x}Ti_x)_2O_7$ into *G*-AFM-I beyond $x = 3\%$ [12–17]. Such simultaneously active lattice, charge, and spin degrees of freedom make Ti-doped $Ca_3Ru_2O_7$ an ideal testbed to explore the correlation physics in complex oxides.

The multiple phases in $Ca_3(Ru_{1-x}Ti_x)_2O_7$ with distinct electrical and magnetic properties [Fig. 1(a)] are analogous to the colossal magnetoresistive (CMR) manganites [18]. As in any first-order phase transitions, the MIT in most CMR systems is accompanied by a mixture of two terminal phases,

which underlies the drastic change of resistivity under external stimuli such as temperature (T), magnetic (B) field, electric current, light, and pressure [19]. In this Rapid Communication, we report the direct visualization of coexisting phases across the Mott transition in 10% Ti-doped bilayer calcium ruthenates using near-field microwave microscopy. Surprisingly, within a narrow range of T and B field near the transition, stripelike metallic domains oriented along the *a* axis, which differ from the two terminal phases, appear inside both the *G*-AFM-I and PM-M regions. Based on the dynamic emergence of the mesoscopic phases and fine features in the macroscopic transport and magnetization data, a phase diagram that includes the phase coexistence can be constructed. Our observation of orientation-ordered phase separation suggests that strongly correlated materials with 4*d* electrons share certain common aspects, while differ in others, with the 3*d* correlated electron systems.

Single crystals of $Ca_3(Ru_{0.9}Ti_{0.1})_2O_7$ in this study were grown by the floating-zone technique [12]. The *T*-dependent magnetic susceptibility (χ) and in-plane resistivity (ρ_{ab}) data with relatively coarse steps (0.05 K for χ and 0.5 K for ρ_{ab}) are plotted in the insets of Figs. 1(b) and 1(c), respectively, showing a single transition from *G*-AFM-I to PM-M at $\sim$113 K upon warming. The results appear to agree with prior investigations on the same $x = 10\%$ material, where no intermediate states between the two phases were found [13,15]. The situation, however, was different when much finer measurements were taken (0.01 K step for χ and 0.1 K for ρ_{ab}), as shown in Figs. 1(b) and 1(c). In the $\chi(T)$ curve, several jumps characteristic for metamagnetic transitions were observed. Within a narrow window in the resistivity data, $\rho_{ab}(T)$ is lower than that of the PM-M phase, reminiscent of the parent compound where the metallic AFM-*a/b* phase develops [6,10]. Figures 1(c) and 1(d) also show the result
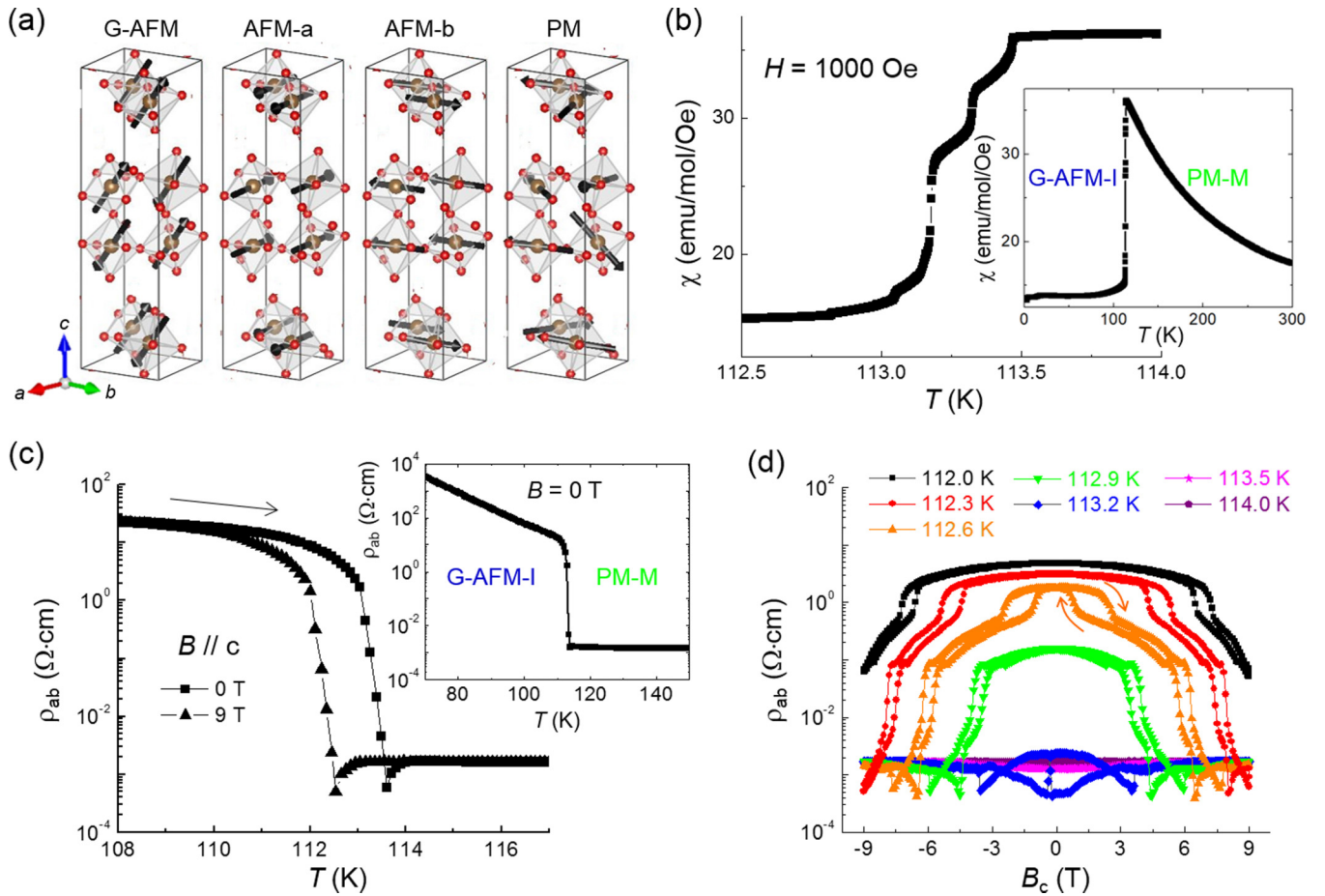
FIG. 1. (a) Schematics of the magnetic structures of (from left to right) G-AFM, AFM-a, AFM-b, and PM phases [10,12]. Only the RuO$_6$ octahedrons are shown here for clarity. (b) Magnetic susceptibility taken under an out-of-plane field of 1000 Oe, showing multiple metamagnetic steps around the transition. The inset shows $\chi(T)$ in a wider temperature range and coarse steps, where only a single transition is observed. (c) In-plane resistivity taken at $B_c = 0$ and 9 T. The inset shows $\rho_{ab}(T)$ at 0 T in a wider temperature range and coarse steps. (d) Magnetoresistivity at various temperatures. The field sweep direction is indicated for the 112.6 K data.

under an out-of-plane B field, which is compatible with our scanning experiment. It should be noted that the spin flip-flop transition for the $B||c$ axis occurs at much higher fields than the $B||a$ or b axis and intermediate states are present throughout the transition [20]. As a result, the effect of B_c in this work is mostly to destroy the G-AFM ordering. The presence of multiple steps and sudden jumps in the magnetoresistance data indicates that the MIT may involve richer physics than previously conjectured. In particular, the resistivity at 113.2 K jumps between 2×10^{-3} Ω cm (PM-M) and a lower value of 4×10^{-4} Ω cm, indicative of the emergence of a new metallic phase near the transition.

In order to explore the real-space evolution of this complex phase transition, we carried out cryogenic microwave impedance microscopy (MIM) [21], as illustrated in Fig. 2(a). The 1 GHz signal is delivered to a tungsten tip (diameter $\sim$100 nm) glued to a quartz tuning fork (TF) for topographic feedback [22,23]. The microwave electronics measure the real (MIM-Re) and imaginary (MIM-Im) parts of the tip-sample admittance, which is demodulated at the TF resonant frequency ($\sim$40 kHz) to form the corresponding AC_MIM images [23]. Figure 2(b) shows the simulated AC_MIM-Im/Re signals as a function of the in-plane resistivity (Sup-

plemental Material Fig. S1 [24]), taking into account the fact that $\rho_{ab} \ll \rho_c$ in this material [15,16]. Even though the low-T phase is insulating, its resistivity near the MIT is still on the conductive side for the 1 GHz MIM [23]. On this side of the response curve, it is easier to distinguish the PM-M and G-AFM-I regions in the MIM-Re channel, where the signal decreases as the sample becomes more conductive, due to the cleaner data and less topographic crosstalk than MIM-Im. In addition, surface particles observed in the topography [Fig. 2(c)] also display vanishing MIM-Re signals. Nevertheless, they are clearly on the resistive side of Fig. 2(b) as their MIM-Im signals are the lowest in the map (Fig. S2 [24]).

The AC_MIM-Re images at various temperatures across the MIT are shown in Fig. 2(d) (complete data in Fig. S2 [24]). Note that the apparent T_{MIT} in Figs. 1 –3 may differ slightly by a few kelvins, depending on the detailed thermal or magnetic-field history of the sample, which is not uncommon for strongly correlated materials. For temperatures much below T_{MIT}, the sample was mostly in the insulating state (phase I), with some highly conductive areas (phase II) observed in the microwave image. Since T_{MIT} decreases as decreasing Ti doping, phase II is likely associated with a local
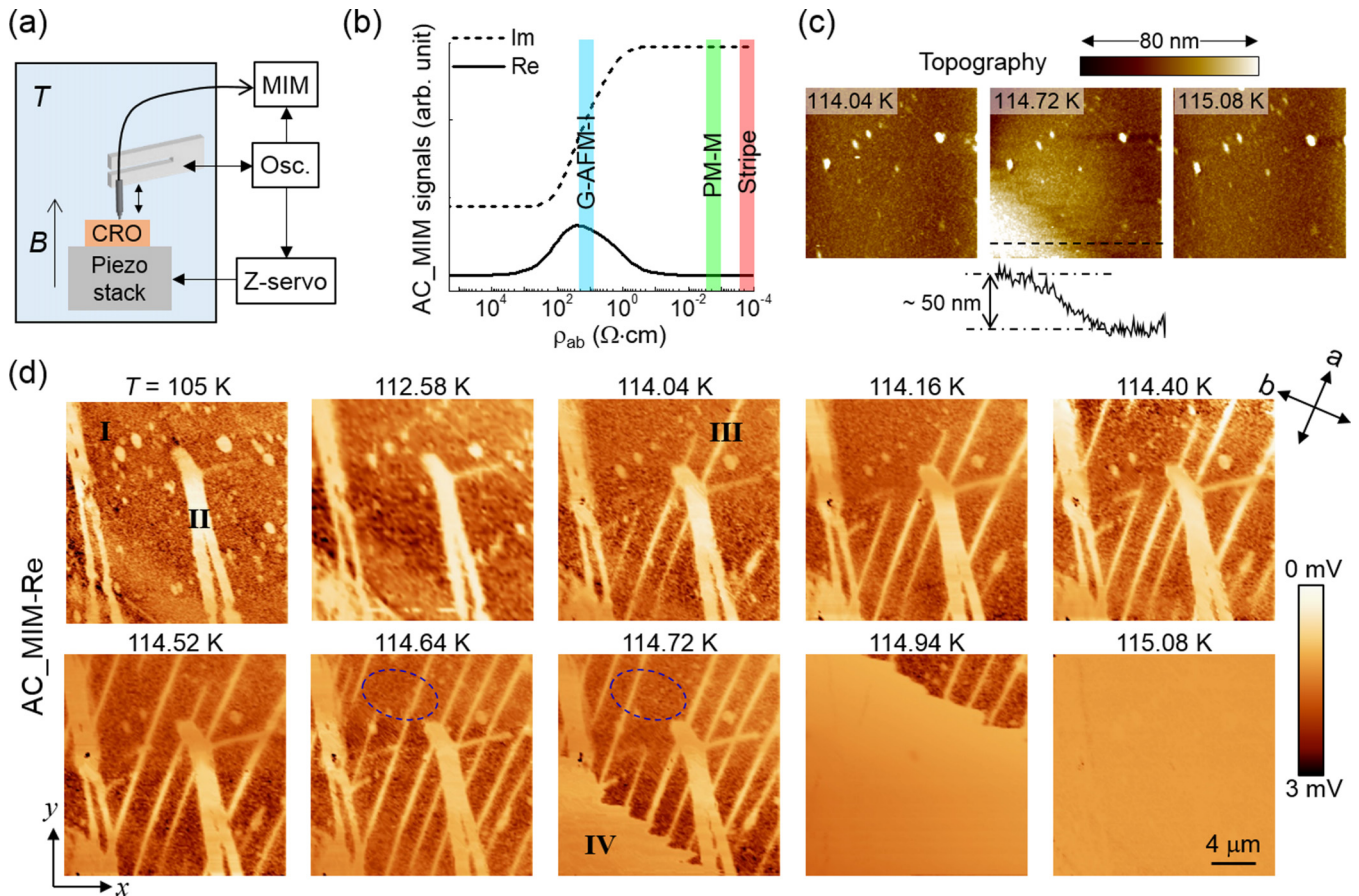
FIG. 2. (a) Schematic of the tuning-fork-based cryogenic MIM setup. The TF electronics control the z scanner and provide the reference to demodulate the MIM signals. (b) Simulated AC_MIM signals as a function of ρ_{ab}. The resistivity values of relevant phases are indicated in the plot. (c) Topographic images at three selected temperatures. Note that the color scale corresponds to the relative height difference within each frame. The inset shows a line profile in the 114.72 K image. (d) AC_MIM-Re images at various temperatures across the transition. Phases I–IV are labeled in the images. The blue ellipses in the 114.64 and 114.72 K images show the dynamic appearance and disappearance of two stripes. The scanning directions (x and y) and the crystalline axes (a and b) are indicated in the bottom left and top right corners, respectively. All images are 20 μm × 20 μm.

deficiency of Ti concentration, which segregates into isolated regions during the floating-zone crystal growth. Since the lattice constant sensitively depends on the Ti doping, such minority phases may self-organize in regular shapes under strain when the crystal is cooled to room temperature, which could explain its ribbonlike shape and orientation along the high-symmetry [110] and [1$\bar{1}$0] directions. Finally, we note that phase II does not exhibit obvious topographic features throughout the phase transition [Fig. 2(c)]. As the c-axis lattice constant is rather different between the G-AFM-I and PM-M phases [12,16], phase II regions in the MIM images must be thin slabs on the surface. One cannot, however, exclude the existence of similar Ti-deficient domains in the interior of the sample.

Starting from 114.04 K, metallic stripes (phase III) were observed in the MIM images, whose length and areal density grew rapidly with increasing T at 0.1 K steps. The stripes are oriented along the a axis of the crystal, as determined by the x-ray diffraction data (Fig. S3 [24]). The width of the stripes ranges from 100 nm (limited by the spatial resolution) to ~1 μm and the spacing between adjacent ones is 3–5 μm. The micrometer-sized separation between the stripes indicates

that the elastic strain between different phases, rather than the electronic correlation, plays a key role here. In particular, the characteristic spacing is likely determined by the length scale at which the strain can be accommodated inside the crystal. The appearance of stripes is dynamic [blue ovals in Fig. 2(d)] and they are not pinned to specific locations in different thermal cycles (Fig. S4 [24]). At 114.72 K, another metallic phase (phase IV) set in, which quickly swept through the scanned area with an additional ~0.3 K. The topographical images in Fig. 2(c) indicate that phase IV is associated with a pronounced increase in height, corresponding to the ~0.1% increase of lattice constant in the c axis across the MIT [12,16]. Phase IV is thus the global PM-M phase that extends through the entire crystal.

Since the MIM contrast between the two possible metallic phases (PM-M and AFM-a/b) is too small, it is not obvious from Fig. 2 whether phase III is the same as II/IV or represents a new electronic state. To enhance the contrast, we have used a blunter tip in a different cool down (Fig. S1 [24]). Figure 3(a) shows the topography and AC_MIM-Re images at $T =$ 111.40 K and $B = 0$ T, from which two rounds of experiments were performed. In Fig. 3(b), the B field was kept at zero
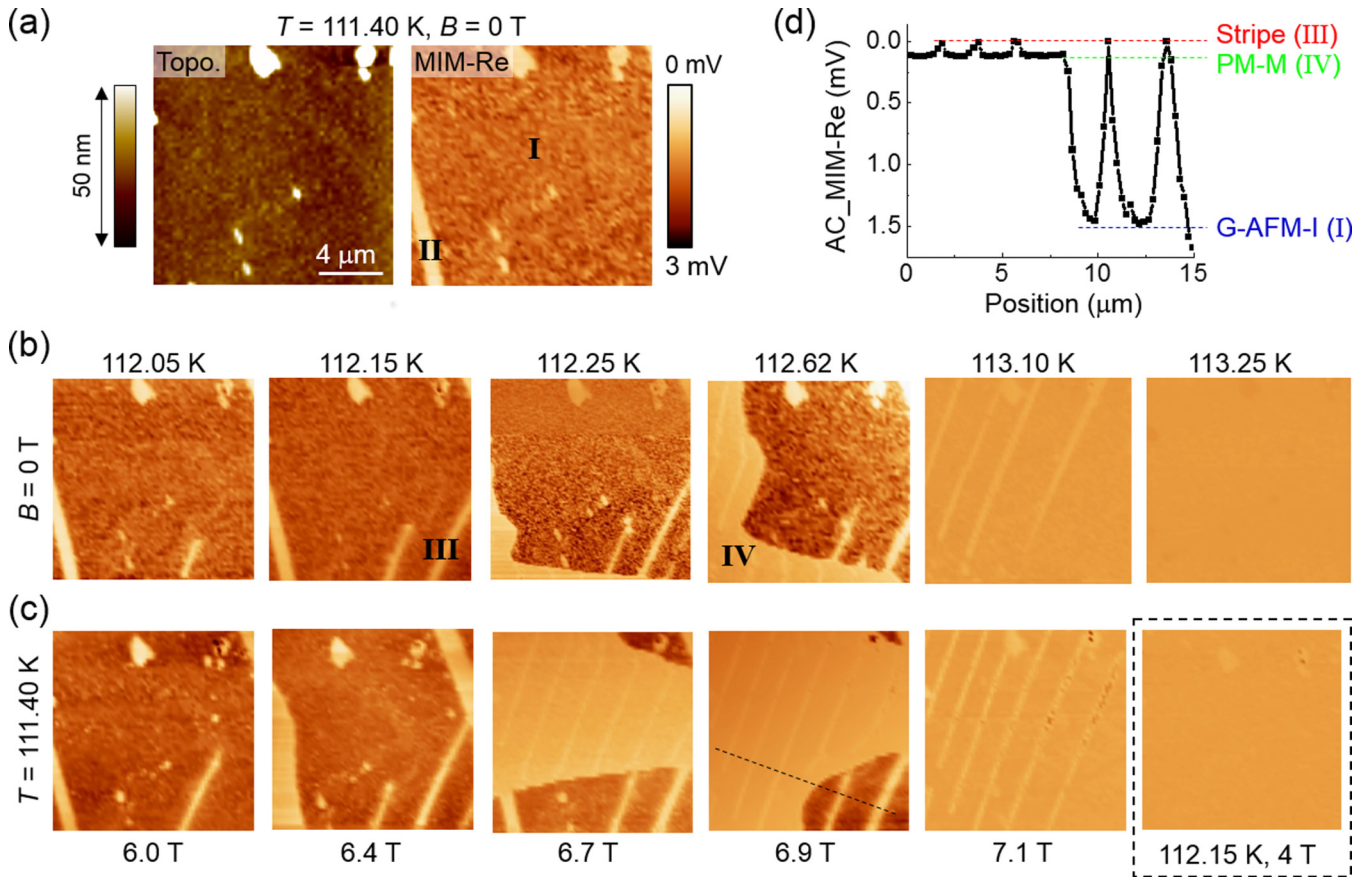
FIG. 3. (a) Topographic and AC_MIM-Re images at 111.40 K and 0 T of a different cool down. (b) MIM images at various temperatures and 0 T. (c) MIM images at various magnetic fields and 111.40 K, except for the last image at a higher temperature and 4 T. Phases I–IV are again labeled in the data. All images are 15 μm $\times$ 15 μm. (d) Line profile in (c), showing the AC_MIM-Re signals across stripes in both the *G*-AFM-I and PM-M phases.

during a warm-up across the transition. Similar to Fig. 2(c), all four phases—I as G-AFM-I, II as local PM-M at lower x, III as the stripes, and IV as the global PM-M—were observed in this area. Strikingly, the stripes could also be seen inside phase IV. The same phenomenon was also observed in Fig. 3(c), where we kept $T = 111.40$ K and ramped up the B field, except for the last image (Fig. S5 [24]). Moreover, the line profile in Fig. 3(d) shows that the stripe domains inside phases I and IV display the same MIM signals. In other words, the stripes are indeed a new electronic state that is distinct from the two terminal phases of the transition. This observation of an additional phase during the metal-insulator transition in strongly correlated materials highlights the complexity in 4d ruthenates. Interestingly, the stripes in the two major phases seem to avoid each other at the boundary (Fig. S6 [24]). Based on the prior knowledge in Ca$_3$(Ru$_{1-x}$Ti$_x$)$_2$O$_7$ [12–17], the stripes are likely the sequential appearance of AFM-a and AFM-b phases during the transition, although we do not have direct evidence on their magnetic ordering. In addition, phase III does not exhibit appreciable topographic contrast over the *G*-AFM-I or PM-M phases, whose lattice constants in the c axis differ by ∼0.1% [12,16]. Since the noise floor of our TF feedback is 2–3 nm, one can infer that the stripes in the MIM images are surface features with a thickness no more than a few microns. Similar to the analysis of phase II, however,

we cannot exclude the appearance of such domains inside the crystal (Fig. S2 [24]).

The mesoscopic MIM imaging allows us to reevaluate the magnetization and transport data and construct a new phase diagram for Ca$_3$(Ru$_{0.9}$Ti$_{0.1}$)$_2$O$_7$ [13,15,25] that includes the nanoscale phase separation. For instance, the magnetotransport curve at 112.6 K [Fig. 4(a)] can be divided into four sections based on sudden changes of the slope, presumably due to the appearance or disappearance of certain coexisting phases. Similar analysis can be applied to the $\rho(T)$ and $\chi(T)$ data in Fig. 1. As shown in Fig. 4(b), the coexistence of the stripe phase with the two terminal phases reveals a complex energy landscape that takes place near the Mott transition in this system.

As a concluding remark, it is instructive to compare our results with nanoscale phase separation in other complex oxides. In the more extensively studied 3d correlated electron systems near MITs, the coexisting phases may exhibit random shapes and sizes [26–30] or orientation-ordered patterns [31–34]. The latter clearly signifies the strong effect of elastic strain on phase transitions. For comparison, stripelike competing phases are commonly seen in single crystals of 4d ruthenate perovskites, such as Ca$_2$RuO$_4$ [35], Mn-doped Sr$_3$Ru$_2$O$_7$ [36], and now Ca$_3$(Ru$_{1-x}$Ti$_x$)$_2$O$_7$. It is possible that, as the on-site Coulomb energy is reduced for the more extended
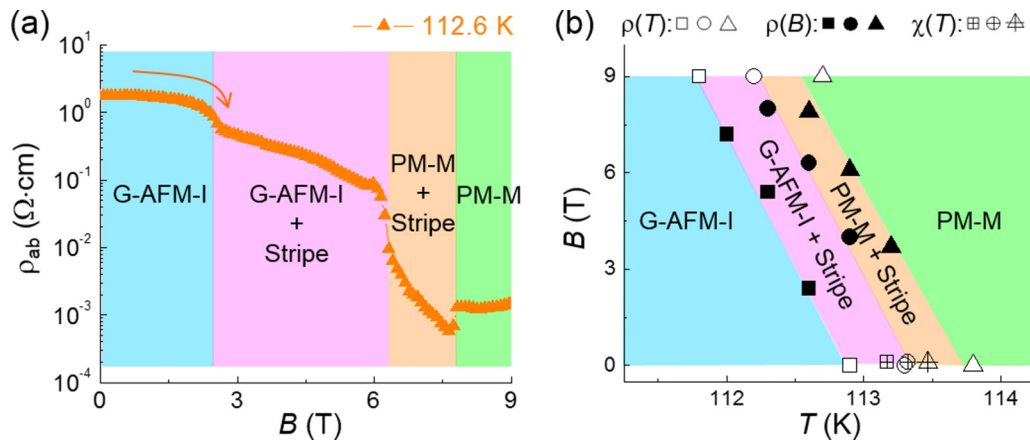
FIG. 4. (a) Magnetotransport curve at $T = 112.6\,\mathrm{K}$ divided into four sections based on sudden changes of the signals. (b) Phase diagram in a narrow temperature and field range taking into account the phase separation. The squares, circles, and triangles ([open, solid, crossed from $\rho(T)$, $\rho(B)$, and $\chi(T)$, respectively) mark the three phase boundaries indicated in the graph. For consistency, all data points are measured on the insulator-to-metal part of the hysteresis loop, i.e., warming up for T dependence and ramping up for B dependence.

$4d$ orbitals with respect to the $3d$ counterpart, the lattice degree of freedom in ruthenates becomes prominent for bulk ruthenate materials. A subtle difference is also expected between different members in the Ruddlesden-Popper series. For instance, stripe domains that are the same metallic phase at the end of the insulator-to-metal transition were also reported in Ca$_2$RuO$_4$ [35], which occur near the physical boundary between the two competing phases. In our case, the stripes, which differ from the two terminal states of the Mott transition, are not confined to the interface between the two global phases. In fact, the effect of phase separation is observable in macroscopic measurements. This new complexity is likely due to the fact that more energetically competing phases are available in the bilayer than single-layer ruthenates.

In summary, we report the nanoscale microwave imaging on doped Ca$_3$(Ru$_{1-x}$Ti$_x$)$_2$O$_7$ through the simultaneous insulator-to-metal and antiferromagnetic-to-paramagnetic transition. Different from the previous picture that a single-step process takes place, we observed a stripelike metallic phase within a narrow temperature and field range of the transition, which is in a different electronic state from the two majority phases. The emergence of such orientation-ordered domains is consistent with the macroscopic transport and magnetization data, suggesting the strong interplay between electronic and lattice degrees of freedom in $4d$ correlated electron systems.

[1] G. Cao, C. S. Alexander, S. McCall, J. E. Crow, and R. P. Guertin, Mater. Sci. Eng. **63**, 76 (1999).

[2] Y. Maeno, H. Hashimoto, K. Yoshida, S. Nishizaki, T. Fujita, J. G. Bednorzt, and F. Lichtenbergtt, Nature (London) **372**, 532 (1994).

[3] R. A. Borzi, S. A. Grigera, J. Farrell, R. S. Perry, S. J. S. Lister, S. L. Lee, D. A. Tennant, Y. Maeno, and A. P. Mackenzie, Science **315**, 214 (2007).

[4] T. He and R. J. Cava, Phys. Rev. B **63**, 172403 (2001).

[5] M. Braden, G. André, S. Nakatsuji, and Y. Maeno, Phys. Rev. B **58**, 847 (1998).

[6] G. Cao, S. McCall, J. E. Crow, and R. P. Guertin, Phys. Rev. Lett. **78**, 1751 (1997).

[7] E. Ohmichi, Y. Yoshida, S. I. Ikeda, N. Shirakawa, and T. Osada, Phys. Rev. B **70**, 104414 (2004).

[8] Y. Yoshida, I. Nagai, S.-I. Ikeda, N. Shirakawa, M. Kosaka, and N. Mori, Phys. Rev. B **69**, 220411(R) (2004).

[9] Y. Yoshida, S.-I. Ikeda, H. Matsuhata, N. Shirakawa, C. H. Lee, and S. Katano, Phys. Rev. B **72**, 054412 (2005).

[10] D. Fobes, J. Peng, Z. Qu, T. J. Liu, and Z. Q. Mao, Phys. Rev. B **84**, 014406 (2011).

[11] F. Baumberger, N. J. C. Ingle, N. Kikugawa, M. A. Hossain, W. Meevasana, R. S. Perry, K. M. Shen, D. H. Lu, A. Damascelli, and A. Rost *et al.*, Phys. Rev. Lett. **96**, 107601 (2006).

[12] X. Ke, J. Peng, D. J. Singh, Tao Hong, Wei Tian, C. R. Dela Cruz, and Z. Q. Mao, Phys. Rev. B **84**, 201102(R) (2011).

[13] J. Peng, X. Ke, G. Wang, J. E. Ortmann, D. Fobes, T. Hong, W. Tian, X. Wu, and Z. Q. Mao, Phys. Rev. B **87**, 085125 (2013).

[14] S. Tsuda, N. Kikugawa, K. Sugii, S. Uji, S. Ueda, M. Nishio, and Y. Maeno, Phys. Rev. B **87**, 241107(R) (2013).

[15] J. Peng, J. Y. Liu, X. Gu, G. Zhou, W. Wang, J. Hu, F. M. Zhang, and X. S. Wu, J. Phys. D: Appl. Phys. **49**, 245004 (2016).

[16] M. Zhu, J. Peng, T. Zou, K. Prokes, S. D. Mahanti, T. Hong, Z. Q. Mao, G. Q. Liu, and X. Ke, Phys. Rev. Lett. **116**, 216401 (2016).

[17] J. Peng, M. Q. Gu, X. M. Gu, G. T. Zhou, X. Y. Gao, J. Y. Liu, W. F. Xu, G. Q. Liu, X. Ke, L. Zhang *et al.*, Phys. Rev. B **96**, 205105 (2017).

[18] Y. Tokura, Rep. Prog. Phys. **69**, 797 (2006).

[19] E. Dagotto, Science **309**, 257 (2005).

[20] S. McCall, G. Cao, J. E. Crow, N. Harrison, C. H. Mielke, A. H. Lacerda, and R. P. Guertin, Physica B **246**, 144 (1998).

[21] W. Kundhikanjana, K. Lai, M. A. Kelly, and Z.-X. Shen, Rev. Sci. Instrum. **82**, 033705 (2011).

[22] Y.-T. Cui, E. Y. Ma, and Z.-X. Shen, Rev. Sci. Instrum. **87**, 063711 (2016).

[23] X. Wu, Z. Hao, D. Wu, L. Zheng, Z. Jiang, V. Ganesan, Y. Wang, and K. Lai, Rev. Sci. Instrum. **89**, 043704 (2018).

[24] See Supplemental Material at http://link.aps.org/supplemental/10.1103/PhysRevB.101.201106 for a finite-element analysis of the MIM signals, a complete set of topography and microwave images, and a detailed analysis of some MIM and the transport data.

[25] J. Peng, J. Y. Liu, J. Hu, Z. Q. Mao, F. M. Zhang, and X. S. Wu, Sci. Rep. **6**, 19462 (2016).

[26] M. Uehara, S. Mori, C. H. Chen, and S.-W. Cheong, Nature (London) **399**, 560 (1999).

[27] M. Fäth, S. Freisem, A. A. Menovsky, Y. Tomioka, J. Aarts, and J. A. Mydosh, Science **285**, 1540 (1999).

[28] W. Wu, C. Israel, N. Hur, S. Park, S.-W. Cheong, and A. de Lozanne, Nat. Mater. **5**, 881 (2006).

[29] M. M. Qazilbash, M. Brehm, B.-G. Chae, P.-C. Ho, G. O. Andreev, B.-J. Kim, S. J. Yun, A. V. Balatsky, M. B. Maple, F. Keilmann *et al.*, Science **318**, 1750 (2007).

[30] K. W. Post, A. S. McLeod, M. Hepting, M. Bluschke, Y. Wang, G. Cristiani, G. Logvenov, A. Charnukha, G. X. Ni, P. Radhakrishnan *et al.*, Nat. Phys. **14**, 1056 (2018).

[31] K. Lai, M. Nakamura, W. Kundhikanjana, M. Kawasaki, Y. Tokura, M. A. Kelly, Z.-X. Shen, Science **329**, 190 (2010).

[32] A. S. McLeod, E. van Heumen, J. G. Ramirez, S. Wang, T. Saerbeck, S. Guenon, M. Goldflam, L. Anderegg, P. Kelly, A. Mueller *et al.*, Nat. Phys. **13**, 80 (2017).

[33] J. Wei, Z. Wang, W. Chen, and D. H. Cobden, Nat. Nanotechnol. **4**, 420 (2009).

[34] M. Liu, A. J. Sternbach, M. Wagner, T. V. Slusar, T. Kong, S. L. Bud'ko, S. Kittiwatanakul, M. M. Qazilbash, A. McLeod, Z. Fei *et al.*, Phys. Rev. B **91**, 245155 (2015).

[35] J. Zhang, A. S. McLeod, Q. Han, X. Chen, H. A. Bechtel, Z. Yao, S. N. Gilbert Corder, T. Ciavatti, T. H. Tao, M. Aronson *et al.*, Phys. Rev. X **9**, 011032 (2019).

[36] T.-H. Kim, M. Angst, B. Hu, R. Jin, X.-G. Zhang, J. F. Wendelken, E. W. Plummer, and A.-P. Li, Proc. Natl. Acad. Sci. U.S.A. **107**, 5272 (2010).